Understanding the role of soot oxidation in gasoline combustion: A numerical study on the effects of oxygen enrichment on particulate mass and number emissions in a spark-ignition

Understanding the Role of Soot Oxidation in Gasoline Combustion: a Numerical Study on the Effects of Oxygen Enrichment on Particulate Mass and Number Emissions in a Spark-Ignition Engine

Distaso E.[1], Amirante R.[1*], Tamburrano P.[1], Reitz R. D.[2]

[1]Department of Mechanics, Mathematics and Management, Polytechnic of Bari, Italy
[2]Engine Research Center, University of Wisconsin-Madison, 1500 Engineering Drive, Madison, WI 53705, USA

*Corresponding Author: Riccardo Amirante Ph.D., Polytechnic of Bari, Italy, riccardo.amirante@poliba.it

Keywords: *Soot Formation and Oxidation; Oxygen-Enriched Combustion; Gasoline Flame Speed Modeling; Particulate Mass and Number Prediction; Spark-Ignition Engine Simulations.*

Abstract

The production of increasingly clean engines has become imperative. More stringent regulations for internal combustion engines are constantly proposed, and recent number-based regulations have become a new challenge, since historically only a mass-based regulation needed to be met. It is known that soot particles detectable at the exhaust of an engine are the results of the competition between the formation of soot precursor species and their oxidation. However, the attention is mainly focused on inhibiting soot precursors formation, and much less research is dedicated at elucidating the benefits achievable from enhancing soot oxidation rates. Soot oxidation can be enhanced by increasing the in-cylinder oxygen content. Oxygenated fuels, which are often added to gasoline in order to achieve more efficient combustion, can represent a possible way for achieving this goal. However, chemical mechanisms are still uncertain for practical fuels, and ambiguous results can be produced when the effect of oxygenated fuels on gasoline engine combustion and soot emissions is considered. In the present study, 3-D Computational Fluid Dynamics simulations were performed and the numerical results were compared with existing experimental data, in which load increases were achieved by pure oxygen addition within the intake manifold of a single-cylinder Spark-Ignition (SI) engine. Studying the effects that an addition of 5% and 10% by volume (with respect to air) of additional oxygen produces on the combustion process, allowed to provide basic additional information on soot formation and oxidation, avoiding the uncertainties associated with chemistry models. A semi-detailed soot model and a chemical kinetic

model, including poly-aromatic hydrocarbon formation, were coupled with the G-equation flame propagation model for SI engine simulations and for predictions of soot mass and particulate number density. Improvements in the modeling of gasoline premixed combustion were achieved, as well. Specifically, different approaches in the evaluation of the laminar flame speed of gasoline (which is a key factor for obtaining reliable SI engine simulations) were critically compared and analyzed. The numerical results showed aspects that were not possible to appreciate by only referring to the experimental results on which this work was based. It was possible to observe that the higher soot concentrations were located in regions characterized by lower temperatures and lower OH concentrations. Oxygen addition favored a faster burning velocity and produced higher in-cylinder temperatures. However, the production rates of both OH radicals and soot precursor species resulted enhanced. The analysis of these concurrent phenomena allowed to explain why in the experiments the soot mass per kg of fuel was lower for the oxygenated combustion cases.

1 Introduction

The recent establishment of a limit on Particle Number (PN) concentration and more stringent limits on Particulate Mass (PM) has increased the efforts putted worldwide into better understanding the production mechanisms of particulate emissions [1–4]. More attention has been focused on developing new emissions reduction strategies, which generally consist of the simultaneous implementation of new combustion techniques [5–7] coupled with innovative control methods [8–10].

In this scenario, it is becoming conventional wisdom that gasoline Spark-Ignition (SI) engines show a wider margin for further improve their efficiency and meet upcoming stringent emission regulations, in comparison to Diesel engines [11, 12]. In fact, the introduction of the high boost and downsizing techniques offers the potential to increase power density and limit pumping and friction losses [13, 14]. Moreover, the gasoline direct injection strategy has recently attracted great interest due to its capability to further improve fuel economy and reduce gaseous emissions [15]. However, the development of such technologies is far from being considered completely mature and is challenging for engine designers [16, 17]. The main limitations are imposed by the occurrence of abnormal combustion modes [18, 19], especially concerning the direct injection technology applied to highly boosted downsized engines operating at low-speed and high-load regimes [20–23].

Oxygen-enriched combustion has been widely studied in order to provide an additional alternative for turbo-charging, especially in the case of downsized SI engines. An oxygen-enriched mixture can serve both as a booster to increase engine output and as a combustion enhancer when the engine operates at low loads or in cold start

conditions. In fact, it has been pointed out that, adding oxygen can results in higher power densities [24–27] low carbon monoxide and hydrocarbon emissions [27–29], as well as it can reduce cold-start emissions [24, 30]. This because the addition of oxygen leads to a decrease in the combustion phase, namely a more complete and quick combustion is achievable [24, 28, 31], also due to less mixing and reaction irreversibilities [25].

Thus, oxygen addition, coupled with downsizing, can ensure a typical requirement for a SI engine in terms of power, but with the advantage of employing a smaller and lighter engine. By controlling the oxygen content, it is possible to optimize the downsized operating mode due to the direct effect on the combustion process and overall engine thermodynamics [24, 25]. However, oxygen-enriched combustion includes some intrinsic drawbacks, that need to be accounted for, such as higher nitrogen oxides emissions, higher in-cylinder and exhaust temperatures, and costs.

An alternative way to meet present emission requirements being considered by several researchers consists in the use of alternative fuels, since it has been found that fuel selection impacts the power output and exhaust emission of vehicles [23, 32]. Therefore, investigating the behavior of alternative fuels, as well as of their mixtures, represents a practical mid-term solution for the automotive marketplace, until more advanced technologies are available and become more economically attractive [33–37].

Oxygenated fuels represent an interesting choice and they are often added to gasoline in order to achieve more efficient combustion. For example, alcohols, such as ethanol, butanol, and their blends with gasoline are considered as valid alternative fuels and have been extensively studied by many researchers [23, 38–41]. In particular, ethanol has become an additive of choice for oxygenated fuels in many places around the world [6, 23, 39, 40]. However, a number of other chemical compounds could be added to the fuel to produce the desired effects [42]. For example, the use of gasoline containing 3 to 10 vol% of bioethanol is being promoted in many parts of the world [43]. Ethanol has the potential to improve engine efficiency and to reduce harmful emissions when used as the fuel in a spark-ignited engine [39, 41]. Kim et al. [40] highlighted that in order to fully utilize the merits of ethanol, the fuel-blending ratio should be changed according to the engine operating conditions. Other advantages include its high octane number and its self-sustainability, since it is obtained from renewable energy sources [41]. However, the effect on particulate emissions is not well understood.

Chemical mechanisms are still uncertain for practical fuels, and ambiguous results can be produced when the effect of oxygenated fuels on gasoline engine combustion is considered [44–46]. To better assess the influence on engine performance and emissions, it is necessary to developed well validated detailed kinetic models for combustion and oxidation of the components of biofuels. In addition, as Tran et al. [44], when reviewed the major detailed kinetic models already proposed in the literature, highlighted that some of the most recent mechanisms can be very large in terms of the species and

reactions involved: for instance, the model of Harper et al. [47] for the oxidation of n-butanol consists of 263 species and 3381 reactions and that of Herbinet et al. [48] for the oxidation of methyl palmytate includes 30425 reactions and 4442 species. More practical and reliable approaches should be taking into account in order to provide more insight on this complex and comparatively new field, which particle characterization from vehicle emissions is.

When the goal is reducing soot emissions, the common thought is that the best way consists in inhibiting the formation of soot precursors. However, it must be highlighted that soot emissions are characterized by two competing in-cylinder processes, namely soot formation and soot oxidation. So that, soot oxidation rates can also have a strong effect on soot emissions levels and improving the oxidation rate can result in beneficial effects [49–52]. Therefore, it should not surprise that previous studies have shown that reducing the formation of soot did not necessarily correlate with a reduction of soot emissions [53], especially when the availability of oxidizers is reduced and hence the oxidation process inhibited.

It is well known that temperature has a strong influence on chemical reaction rates. In the case of soot, it has been observed that the rate of the reactions involved in soot oxidation increase faster with temperature than those of the reactions responsible for soot formation [54]. An interesting result pointed out by Gallo et al. [49] indicates that global turbulence levels are not necessarily beneficial. By means of laser extinction measurements carried out on an optical heavy-duty diesel engine, they found that varying swirl and engine speed produced ambiguous trends. A possible explanation provided in that work was based on the supposition that soot formation extremely depends on local conditions, which means that turbulence needs to be increased at the specific locations where soot is oxidized for obtaining appreciable effects.

In the present study, in order to provide additional basic information and, at the same time, to avoid uncertainties from chemistry models, load increases in stoichiometric SI engine combustion were achieved by pure oxygen addition as a first step. 3-D Computational Fluid Dynamics simulations were performed and the numerical results were compared with existing experimental data carried out by Catapano et al. [27], in which 5% and 10% by volume of additional oxygen (with respect to air) was mixed with gasoline within the intake manifold of a small single-cylinder Port Fuel Injection SI engine. Different engine operating conditions were also considered for a more exhaustive analysis.

For the numerical study, the KIVA3V Release 2 code, coupled with a Jacobian Chemistry solver, SpeedCHEM, was used [55]. The semi-detailed soot model of Vishwanathan et al. [56] with Jiao and Reitz's improvements [57] and a chemical kinetic mechanism that includes iso-octane/n-heptane/toluene/PAH [58], were coupled with the Discrete Particle Ignition Kernel model [59] and the G-equation flame propagation

model [60, 61] for the Spark-Ignition engine simulations and for predictions of soot mass and particulate number density. In addition, a discrete multi-component fuel surrogate approach was used to model the physical and chemical properties of real gasoline, as proposed in [58]. A more accurate formulation for predicting the laminar flame speed of gasoline, which is a vital scaling factor for a successful SI engine simulation, was employed in the present work [62]. For achieving this purpose, different approaches available in the literature for evaluating the laminar flame speed were compared and critically analyzed.

Two different engine speeds were considered for the simulations, namely 2000 and 4000 rev/min, which were assumed to be representative, respectively, of low and high engine speed regimes. In accordance with the experimental tests, beside the baseline conditions, the effects of increasing the initial oxygen content by 5% and 10% were investigated. For the low-speed case, the results were further analyzed to provided in-cylinder soot distributions and to better understand the reasons for the experimentally observed soot particle size distributions.

2 Modeling approach

The multi-dimensional KIVA-3V code developed at the Los Alamos National Laboratory [63–65] was used for the present modeling work. In particular, the modified version of KIVA-3V developed at the Engine Research Center (ERC) of the University of Wisconsin-Madison was adopted and includes improvements in its ignition, combustion and emission models.

The KIVA code was coupled with the SpeedCHEM code [55], where KIVA models the fuel preparation, the governing equations for using conservation of mass, momentum and energy, as well as species transport, and SpeedCHEM solves the gas phase fuel chemistry. The chemistry solver is called for each cell and the fuel chemistry is modeled using a kinetic reaction mechanism that contains the species and thermodynamic data for a given fuel, as well as reactions and reaction rates information that describe the oxidation process. Each computational cell is considered to be a Well-Stirred Reactor (WSR), and the production rates for each species are calculated and used with the mass fraction, density, and molecular mass to form new species based on the reactions in the mechanism. Species concentration changes are returned to KIVA and these values are used to calculate the energy release at each time step in the calculation.

The main sub-models used for the SI engine simulation are briefly described here, together with the improvements made for a more accurate evaluation of gasoline flame propagation, essential to correctly predict combustion phasing and in-cylinder pressure evolution.

2.1 Spark-ignition model

In a SI engine the combustion process is initiated as a point-source ignition kernel by the triggering of the spark and then governed by the subsequent flame propagation phenomenon.

Although the early stage of ignition is important, it is not practical to resolve the process in detail in engine CFD simulations, because the typical grid-size and time step used is larger than that needed to describe this early stage of ignition precisely. Thus, a relatively simple sub-grid scale model is needed to simulate the early ignition process. In the present work, the growth of the ignition kernel is tracked by using the so-called Discrete Particle Ignition Kernel (DPIK) model developed by of Fan et al. [59] and improved by Tan and Reitz [61].

In the DPIK model, following a Lagrangian approach, the ignition kernel is represented by particles that move radially outwards from the spark-plug electrodes. The kernel grows by keeping a spherical shape and its growth rate depends upon several parameters, i.e., the mixture strength, the turbulence intensity, the spark discharge energy, the gas temperature and pressure. Assuming the temperature inside the kernel to be uniform, the kernel growth rate is:

$$\frac{dr_{ker}}{dt} = \frac{\rho_u}{\rho_{ker}} \left(S_{plasma} + S_T \right), \tag{1}$$

where r_{ker} is the kernel radius, ρ_u is the local unburnt gas density, S_T is the turbulent flame speed, and ρ_{ker} is the gas density inside the kernel region. Based on the energy balance analysis of the ignition kernel thermodynamic system, the plasma velocity S_{plasma} is given as [61]:

$$S_{plasma} = \frac{\dot{Q}_{spk}\eta_{eff}}{4\pi r_{ker}^2 \left[\rho_u \left(u_{ker} - h_u \right) + p\frac{\rho_u}{\rho_{ker}} \right]}, \tag{2}$$

where $\dot{Q}_{spk}$ is the electrical energy discharge rate, η_{eff} is the electrical energy transfer efficiency due to heat loss to the spark plug. $\eta_{eff} = 0.3$, as suggested by Heywood [66] is used in this study. ρ_u and h_u are the density and specific enthalpy of the unburnt mixture, respectively. ρ_{ker} and u_{ker} are the density and internal energy of the mixture inside the kernel.

To account for turbulent strain and curvature effects on the kernel flame, the unstretched laminar flame speed S_L^0 was multiplied by a stretch factor, following the form proposed by Herweg et al. [67] (cf. [59, 61]).

For the cells that do not contain the kernel flame particles, the chemical source terms are calculated by detailed chemistry based on the WSR assumption

2.2 Transition from kernel growth to turbulent flame propagation

The DPIK model is used when the flame is not significantly disturbed by the turbulence. However, when the kernel size exceeds a critical diameter, a the transition from the kernel growth model to the actual turbulent flame propagation calculation is required. This transition follows the criteria introduced by Liang and Reitz [68], and it is based on the local turbulent integral length scale, l, of the flow, viz.:

$$r_k \geq C_m l = C_m \cdot 0.16 \cdot \frac{k^{\frac{3}{2}}}{\varepsilon} \tag{3}$$

where k and e are the turbulent kinetic energy and its dissipation rate, respectively. C_m is the only model constant that needs to be tuned within the code used for the present work.

2.3 G-equation model

The G-equation model is than called for calculating the turbulent flame front evolution. Based on a flamelet approach, it assumes that the burnt and unburnt gases are separated by the flame brush, which is modeled as a 3-dimensional surface, defined by the equation $G(\boldsymbol{x}, t) = 0$. This surface divides the flow field into an unburnt region, $G < 0$, and a burnt gas region, $G > 0$.

The G-transport equation formulated by Peters [69], valid in both *thin reaction zone* and *corrugated flamelets* regimes, was adopted:

$$\rho \frac{\partial G}{\partial t} + \rho \mathbf{u} \cdot \nabla G = \left(\rho S_L^0\right) \sigma - (\rho D)\, \kappa \sigma, \tag{4}$$

where $\boldsymbol{u}$ is the bulk fluid velocity of the unburnt mixture ahead of the flame front, ρ its density, S_L^0 the unstretched planar laminar flame speed, κ the flame curvature and σ is the turbulent to laminar flame surface area ratio or equivalently the flame speed ratio, i.e.,

$$\sigma = \frac{A_T}{A_L} = \frac{S_T^0}{S_L^0} = 1 + \frac{S_T^0 - S_L^0}{S_L^0} = |\nabla \tilde{G}| + \sigma_T, \tag{5}$$

and σ_T accounts for the turbulent contribution to the flame surface area ratio σ. More information about the terms appearing in Equations (4) and (5), as well as their derivation, can be found in [69].

Based on Equation (4), a set of Favre-averaged level set equations applicable to both regimes can be derived, including the equations for the Favre mean, $\tilde{G}$, and its variance, $\widetilde{G''^2}$, and a model equation for the flame surface area ratio σ_T. These equations, together with the Reynolds averaged Navier-Stokes equations and the $k - \epsilon$ turbulence modeling equations, form a complete set to describe premixed turbulent flame front

propagation [69]. Considering the Arbitrary Lagrangian-Eulerian (ALE) numerical method used in the KIVA code, the equation set, accounting for the change of $\tilde{G}$ value due to the velocity of the moving vertex, $\mathbf{u}_{vertex}$ [70], suitable for KIVA implementation, is:

$$\frac{\partial \tilde{G}}{\partial t} + (\tilde{\mathbf{u}} - \mathbf{u}_{vertex}) \cdot \nabla \tilde{G} = \frac{\bar{\rho}_u}{\bar{\rho}} S_T^0 |\nabla \tilde{G}| - D_T \tilde{\kappa} |\nabla \tilde{G}|, \tag{6}$$

$$\frac{\partial \widetilde{G''^2}}{\partial t} + \tilde{\mathbf{u}} \cdot \nabla \widetilde{G''^2} = \nabla_{\|} \cdot \left(\frac{\bar{\rho}_u}{\bar{\rho}} D_T \nabla_{\|} \widetilde{G''^2} \right) + 2 D_T (\nabla \tilde{G})^2 - c_s \frac{\tilde{\varepsilon}}{\tilde{k}} \widetilde{G''^2} \tag{7}$$

$$\bar{\rho} \frac{\partial \bar{\sigma}_T}{\partial t} + \bar{\rho} \tilde{\mathbf{u}} \cdot \nabla \bar{\sigma}_T = \nabla_{\|} \cdot \left(\bar{\rho} D_T \nabla_{\|} \bar{\sigma}_T \right) + c_0 \bar{\rho} \frac{\left(-\widetilde{\mathbf{u}'' \mathbf{u}''} \right) : \nabla \tilde{\mathbf{u}}}{\tilde{k}} \bar{\sigma}_T + c_1 \bar{\rho} \frac{D_T (\nabla \tilde{G})^2}{\widetilde{G''^2}} \bar{\sigma}_T - c_2 \bar{\rho} \frac{S_L^0 \bar{\sigma}_T^2}{\left(\widetilde{G''^2} \right)^{1/2}} - c_3 \bar{\rho} \frac{D \bar{\sigma}_T^3}{\widetilde{G''^2}}, \tag{8}$$

where $\nabla_{\|}$ is the tangential gradient operator, $\mathbf{u}$ the fluid velocity, $\mathbf{u}''$ the turbulence intensity, D_T the turbulent diffusivity, and c_s, c_0, c_1, c_2, and c_3 are modeling constants (cf. Ref. [69]), $\tilde{k}$ and $\tilde{\varepsilon}$ are the Favre mean turbulent kinetic energy and its dissipation rate from the RNG $k - \varepsilon$ model [71]. $\tilde{\kappa}$ is the Favre mean flame front curvature defined as

$$\tilde{\kappa} = \nabla \cdot \left(\frac{\nabla \tilde{G}}{|\nabla \tilde{G}|} \right). \tag{9}$$

2.4 Primary heat release and species conversion within the turbulent flame brush

The information about the flame front position allows the calculation of the species conservation rate in the flame-containing cells and, consequently, the associated primary heat release at the flame front. In the code, a method based on the sub-grid scale unburnt/burnt volumes [60] was implemented for this purpose. Namely, the sub-grid scale volumes are tracked each time step based on the coordinate information of the cell vertices and the flame surface piercing points. The species density conversion rate then is expressed as:

$$\frac{\partial \rho_i}{\partial t} = \rho_u \left(Y_{i,u} - Y_{i,b} \right) \frac{A_{f,i4}}{V_{i4}} S_l^0, \tag{10}$$

where the $Y_{i,u}$ and $Y_{i,b}$ are the mass fractions of species i in the unburnt and burnt mixtures, respectively. A_f is the mean flame front area and V is the cell volume, $i4$ is the cell index used in the KIVA code.

Chemical reaction mechanisms are applied to model the secondary heat release and pollutant formation within the diffusion flames behind the flame front. Specifically, a reduced chemical kinetic mechanism that includes iso-octane/n-heptane/toluene/PAH

(89 species and 506 reactions) [58] was used in this study for this purpose.

2.5 Semi-detailed soot model

The semi-detailed soot model by Vishwanathan et al. [56], with Jiao and Reitz's improvements [57] was coupled with the above-mentioned chemistry mechanism, for accounting for the nucleation of soot particles from PAH. The smallest incipient particle size is assumed to start from 1.25 nm (size of 100 carbon atoms).

The soot particles, $C_{(s)}$, are assumed to be formed from the PAH species pyrene (A_4) via the reaction

$$C_{16}H_{10}(A_4) \xrightarrow{\dot{\omega}_1} 16C_{(s)} + 5H_2, \qquad \dot{\omega}_1 = k_1[A_4], \quad k_1 = 2000, \tag{11}$$

where $[A_4]$ represents the concentration of A_4 in mol/cm^3, and k_1 has units of $[1/s]$.

Once formed, the particles grow via the *Hydrogen Abstraction-C_2H_2 Addition* (HACA) mechanism:

$$C_{(s)} + C_2H_2 \xrightarrow{\dot{\omega}_2} 3C_{(s)} + H_2, \qquad \dot{\omega}_2 = k_2[C_2H_2], \tag{12}$$

where

$$k_2 = 9.0 \cdot 10^4 e^{-12100/T} \cdot \sqrt{S}, \qquad with \quad S = \pi d_p^2 N, \tag{13}$$

where S is the soot surface area per unit volume in $[1/cm]$, d_p is the particle diameter, and N is the soot number density in $particles/cm^3$.

The soot species density can be correlated with soot particle number density based on mass conservation in each computational cell, via.,

$$\left(\frac{\pi}{6} d_d^3 \rho_{C_{(s)}}\right) n = Y_{C_{(s)}} \rho V, \tag{14}$$

where $n = N\forall$, is the number of particles in a cell, and V is the volume of the cell. $\rho_{C_{(s)}}$ is the soot density for which the density of graphite ($2.0\, g/cm^3$) is used throughout this study, and ρ is the ambient density, Y_{C_s} is the soot mass fraction.

In addition, soot growth is modeled via PAH condensation from

$$C_s + PAH_{k,j} \rightarrow C_{(s+k)} + \frac{j}{2} H_2. \tag{15}$$

PAHs up to four rings ($A_1 \sim A_4$) are included in the current chemistry mechanism, and they also participate in the soot surface growth.

A decrease of particle number density is assumed to occurring during particle coagulation processes, which is modeled using the normal square dependence. The soot particles coagulate following:

$$nC_s \xrightarrow{\dot{\omega}_3} C_{(s)_n}, \tag{16}$$

Table 1: Considered steps in soot formation and oxidation. $C_{(s)}$ represents soot, $PAH_{k,j}$ is a PAH species with k carbon and j hydrogen atoms.

Step	**Reactions**
Soot inception	$C_{16}H_{10}(A_4) \rightarrow 16C_{(s)} + 5H_2$
Soot surface growth	$C_{(s)} + C_2H_2 \rightarrow 3C_{(s)} + H_2C_{(s)} + PAH_{k,j} \rightarrow C_{(s+k)} + \frac{j}{2}H_2$
Soot coagulation	$nC_{(s)} \rightarrow C_{(s)n}$
Soot oxidation	$C_{(s)} + 0.5O_2 \rightarrow CO \qquad C_{(s)} + OH \rightarrow CO + 0.5H_2$

with

$$\dot{\omega}_3 = k_3 \left[\frac{\rho Y_{C_{(s)}}}{M_{C_{(s)}}}\right] [N]^{11/6} \tag{17}$$

and

$$k_3 = 2C_a \left(\frac{6M_{C_{(s)}}}{\pi \rho_{C_{(s)}}}\right)^{1/6} \left(\frac{6k_b T}{\rho_{C_{(s)}}}\right)^{1/2}, \tag{18}$$

where $M_{C_{(s)}}$ is the molecular weight of carbon, C_a the constant is the agglomeration constant with the value of 9.0 suggested by Leung et al. [72] used in this work. Generally, this step reduces the soot number density. k_b is Boltzmann's constant ($1.38054 \cdot 10^{-16}\ erg/K$). It can be observed from Equations 17 and 18 that the soot coagulation rate depends on particle number density and the temperature in each CFD computational cell.

Oxidation occurs by O_2 and OH following:

$$\begin{aligned} C_{(s)} + \frac{1}{2}O_2 &\xrightarrow{\dot{\omega}_5} CO \\ C_{(s)} + OH &\xrightarrow{\dot{\omega}_6} CO + \frac{1}{2}H_2 \end{aligned} \tag{19}$$

where the reaction rates of O_2 and OH oxidation are $\dot{\omega}_5$ and $\dot{\omega}_6$, respectively.

All steps for soot formation and oxidation are summarized in Table 1.

The soot species density and soot number density are treated as passive species in the model, and their transport equations are represented as:

$$\frac{\partial \mathrm{M}}{\partial t} = -\boldsymbol{\nabla} \cdot (\mathrm{M} \cdot \mathrm{v}) + \boldsymbol{\nabla} \cdot \left(\frac{\mu}{SC} \cdot \boldsymbol{\nabla} \left(\frac{M}{\rho}\right) + \varsigma M \frac{\mu}{\rho} \frac{\boldsymbol{\nabla} \mathrm{T}}{T}\right) + \dot{S}_M \tag{20}$$

where M stands for either soot species density $\left(Y_{C_{(s)}} \cdot \rho\right)$in g/cm^3 or soot number density (N) in $partiles/cm^3$. v (cm/s) is the CFD gas-phase velocity, SC is the Schmidt number, μ is the fluid viscosity, T is the temperature of the CFD computation cell, and $\dot{S}_M$ represents source terms.

Details of the steps of the soot model and the source terms for both soot species density and soot number density are described by Vishwanathan [56]. Additionally, source terms for (A_2~A_4) PAH-surface-growth-assisted steps are also included in the

source terms, since they are considered in the current soot model [57].

It must be highlighted that in the present soot model the soot particles are assumed to be spherical and with a single possible size and number density allowed in each computational cell. In this way, the model is locally mono-disperse (on a cell basis). However, the soot diameter and number density can vary from one computational cell to another through the transport equations of both the soot species density and soot number density.

2.6 Gasoline modeling

As showed above, the prediction of the turbulent burning velocity plays an essential role in modeling SI engine combustion. The most crucial scaling factor that affects the reliability of the G-equation model is represented by the laminar flame speed, as can be inferred by the relationship that links the turbulent flame speed S_T^0 to the estimated value for the laminar flame speed S_L^0 in the G-equation model, namely:

$$\frac{S_T^0}{S_L^0} = 1 + I_P\left\{-\frac{a_4 b_3^2}{b_1}\frac{\ell_I}{\ell_F} + \left[\left(\frac{a_4 b_3^2}{b_1}\frac{\ell_I}{\ell_F}\right)^2 + a_4 b_3^2 \frac{u'\ell_I}{S_L^0 \ell_F}\right]^{1/2} I_P\right\} \tag{21}$$

(specific information about the terms appearing in Equation (21) can be found in [68]).

The laminar flame speed is an intrinsic property of the fuel mixture, which therefore means that it is uniquely defined once the unburnt mixture composition, temperature and pressure are known. Encouraging progress has been made in developing detailed chemical kinetic models for its prediction, but such models are still extremely complex and require significant computational effort [73]. Thus, experimental-derived analytical correlations are preferred in engine practical simulations. Such empirical correlations are also more easily implemented in CFD codes than tabulated data. Their implementation allows to restrict the use of detailed chemical kinetics to the solely modeling of the post-flame and the end-gas chemistry, which does not require high resolution, thus saving computational time [74].

The most widespread used form for an empirical correlation is the so-called "power law" formula:

$$S_L^0\left(\phi, T_u, p_u\right) = \ S_{L0}\left(\frac{T_u}{T_0}\right)^{\alpha}\left(\frac{p_u}{p_0}\right)^{\beta}, \tag{22}$$

where S_{L0} is the velocity measured at $T_u = T_0$ and $p_u = p_0$ for a given equivalence ratio ϕ, and α and β are mixture strength-dependent terms.

One of the most widely used correlation having this form was derived by Metghalchi et al. [75] in 1982, from measurements carried out in a constant volume vessel for fuel-air equivalence ratios $\varphi = 0.8 \div 1.5$, over pressure and temperature ranges of $p_u = 0.4 \ \div 50 \ atm$ and $T_u = 298 \ \div 750 \ K$, for methanol, propane, iso-octane and

indolene. They found that the reference velocities S_{L0} could be fit by a second-order polynomial of the form:

$$S_{L0}(\phi) \;=\; 26.32 \;-\; 84.72(\phi - 1.13)^2. \tag{23}$$

The fuel-type independent exponents α and β were represented by the expressions:

$$\begin{aligned} \alpha(\phi) &= 2.18 - 0.8(\phi - 1) \\ \beta(\phi) &= 0.16 \;+\; 0.22(\phi - 1). \end{aligned} \tag{24}$$

In Equation (22) they considered $p_0 = 1\ atm$ and $T_0 = 298\ K$, and recommended expressions for application in the ranges: $p_u = 1 \div 50\ atm$ and $T_u = 350\ \div 700\ K$.

Although the Metghalchi et al. formulation [75] for the reference velocities S_{L0} has gained a lot of popularity (it has been used in many numerical studies, even in the case of fuels that were not those for which it was validated) has the drawback of predicting negative flame speeds for very lean or very rich mixtures. In addition it was not developed specifically for gasoline, so that the use of the value derived for iso-octane, as surrogate, can produce ambiguous results.

A practical solution to the intrinsic problem of that polynomial form, was proposed in 2006 by Liang and Reitz [68], who suggested the use of Gülder's correlation [76] (1984) for the room temperature burning velocity S_{L0}, which has the following form:

$$S_{L0}(\phi) = \; W\ \phi^{\eta}\ e^{-\xi(\phi-\sigma)^2}, \tag{25}$$

where W, η, ξ and σ are constants for a given fuel. In their study, Liang and Reitz [68] correlated the experimental data for iso-octane by Metghalchi et al. [75] within the range $\varphi = 0.65 \div 1.6$, obtaining the following expression for Equation (25):

$$S_{L0}(\phi) = \; 26.9\ \phi^{-0.134}\ e^{-3.86(\phi-1.146)^2}. \tag{26}$$

The same coefficients for exponents α and β proposed by Metghalchi et al. for iso-octane [75] were used [68].

Liang and Reitz used the derived correlation for studying a stratified charge two-stroke gasoline engine, obtaining good agreement with measured data [68]. However, more recently, the same correlation was employed by Jiao and Reitz (2014) to simulate a four-stroke gasoline SI engine under premixed conditions [57], and the results were not as good as for the former case. In this study, to reproduce the characteristics of a EPA Tier II EEE gasoline, in the simulations, the fuel was modeled as a surrogate binary mixture of iso-octane and toluene. However, the ignition timing, as well as the equivalence ratio, were adjusted case-by-case in order to match the C/O ratio of the Tier II EEE certification and, mostly, for reproducing the experimental in-cylinder

pressure traces. The discrepancies were mainly attributed to the flame propagation speeds, which were not in accordance with the experimental values.

In the work by Liang and Reitz [68] pure iso-octane was used in the simulations, but it was not provided any chemical or physical specification related to the gasoline used in the experiments. It is hard to infer any general result regarding flame propagation from this study, because the working operation of the two-stroke DISI engine used in the work is heavily influenced by the mixture preparation and the spray-related processes.

In the case of the four-stroke Port Fuel Injection engine used in the work by Jiao and Reitz [57], in which fully-premixed conditions reign (and the combustion process is exclusively governed by the turbulent flame propagation phenomenon), it was necessary to adjust some parameters, in order to compensate the inaccuracies relying on the evaluation of the laminar flame speed. This depends upon the fact that the analytical correlation used for predicting the flame speed of commercial gasoline, was actually derived for iso-octane, which cannot be considered a reasonable surrogate of gasoline in terms of laminar flame speed.

More recently, Amirante et al. [62] (2017) proposed a specific formulation for gasoline. It was developed on the basis of experimental measurements obtained by several workers and available in the literature. The correlation has the "power law" form of Equation (22), with $p_0 = 1\ atm$ and $T_0 = 298\ K$. The $S_{L0}(\phi)$ term is represented by using "Gülder's exponential formulation" of Equation (25), and the data fitting produced the following expression:

$$S_{L0}(\phi) = \ 36.82\ \phi^{-0.20}\ e^{-6.45(\phi-1.08)^2}. \tag{27}$$

For the exponents α and β a second-order polynomial fitting was proposed:

$$\begin{aligned} \alpha(\phi) &= 3.28\phi^2 - 7.52\phi + 5.93 \\ \beta(\phi) &= -0.925\phi^2 + 2.012\phi - 1.365. \end{aligned} \tag{28}$$

The latter polynomial form for α and β can better reproduce the influence of pressure and temperature on the lean and rich sides, in comparison to the linear expression proposed by Metghalchi et al. [75] and used by Liang and Reitz [68] and Jiao and Reitz [57]. This because Metghalchi et al.'s expression [75] was derived by considering only three different equivalence ratios near stoichiometric conditions [62].

Figure 1 shows a comparison between the results obtainable by employing the analytical correlations developed by Amirante et al. [62] (Equations (27) and (28)), Liang and Reitz [68] (Equations (26) and (24)) and Metghalchi et al. [75] (Equations (23) and (24)). The comparison is made against data collected in two different studies, namely, the work by Sileghem et al. [77], who recently measured the laminar burning velocities for a gasoline Exxon 708629-60 using the heat flux method on a flat flame adiabatic burner

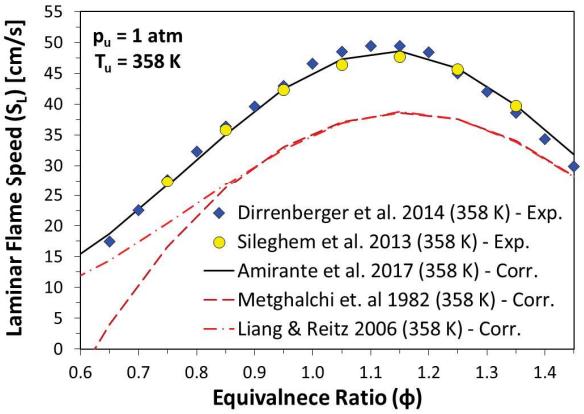

Figure 1: Comparisons between the effectiveness in reproducing experimental measurements of gasoline laminar flame speed of the analytical correlations by Amirante et al. [62], Liang and Reitz [68] and Metghalchi et al. [75].

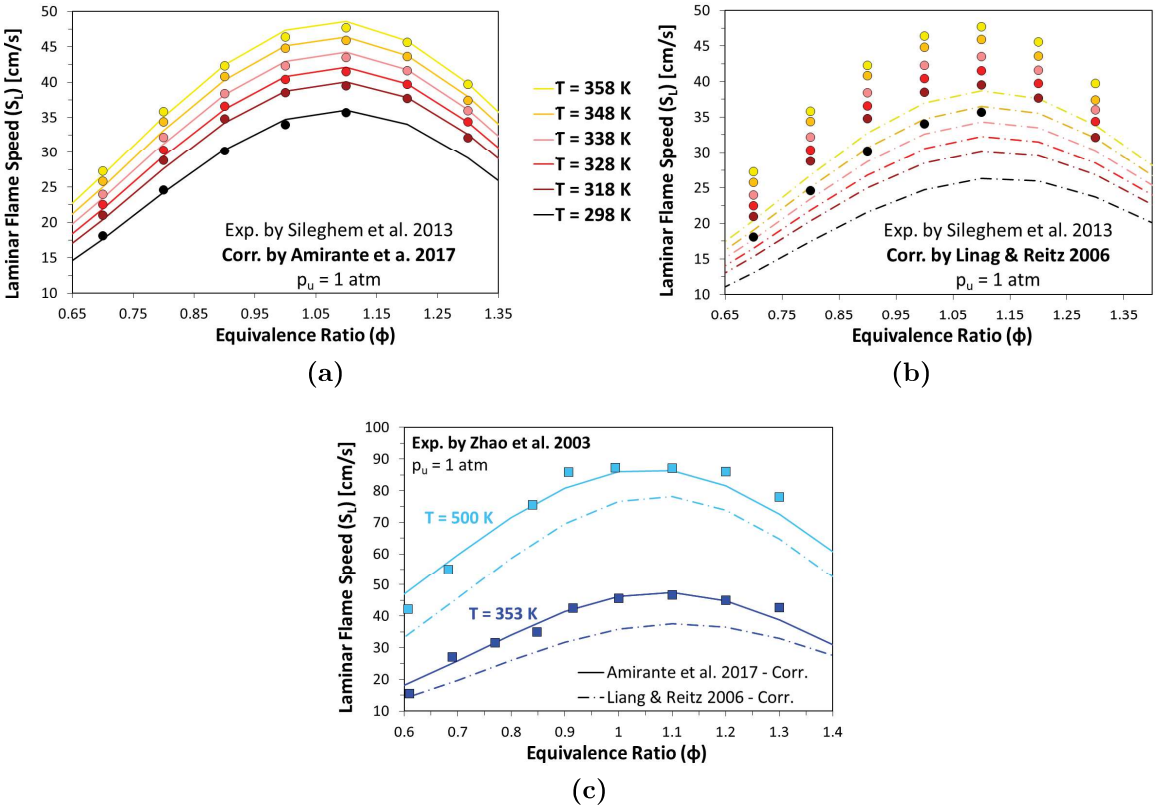

Figure 2: Improvements obtained by Amirante et al. [62] (solid lines), with respect to the correlation by Liang and Reitz [68] (dashed lines), in reproducing the laminar flame speed of commercial gasoline over a wide range of operating conditions. Comparison with the experiments by Sileghem et al. [77] (a) and (b); comparison with the experiments by Zhao et al. [78] (c).

and the data of Dirrenberger et al. [79], who used the same measurement method and found good agreement with the previous study. Figure 1 highlights the improvements made by Liang and Reitz [68] in avoiding negative flame speeds, but shows as well that the values derived for iso-octane are not suitable for reproducing the laminar flame

Table 2: Composition of the surrogate mixture of ten components used to model gasoline in the simulations.

Component	**Mole fraction**
nC_7H_{16}	0.055399
$nC_{10}H_{22}$	0.039687
$C_{10}H_{22}$	0.019337
iC_5H_{12}	0.411976
iC_7H_{16}	0.130568
iC_8H_{18}	0.074380
C_7H_8	0.101062
mxylene	0.062182
mcymene	0.073237
C_6H_{12}	0.032171

speed of gasoline.

Figures 2a and 2b provide a comparison with other experiments carried out by Sileghem et al. [77] at different initial temperatures, confirming that the errors deriving from the use of the correlation of Liang and Reitz [68] cannot be acceptable. Figure 2c refers to the experiments by Zhao et al. [78] who used the stagnation jet-wall flame configuration and Particle Image Velocimetry for measuring the laminar flame speed of a commercial gasoline at higher temperatures than those investigated in the two previous works. The results underline the need of a dedicated formulation for calculating the laminar flame speed of gasoline.

Recently, Teodosio et al. [80] assessed the relative impact that different formulations for predicting the laminar flame speed of gasoline (including those developed by Metghalchi et al. [75] and by Amirante et al. [62]) can have on the prediction of the combustion process in a SI engine. The results highlighted the reliability of the formulation proposed by Amirante et al. [62], which produced trends really close to those obtained by a chemical kinetic solver.

In the present work, the analytical correlation developed by Amirante et al. [62] (Equations (27) and (28)) was implemented in the code for reproducing the flame speed of gasoline. The surrogate mixture of ten components reported in Table 2 was used for reproducing the chemical and physical properties of gasoline used in the experiments and whose specification are reported in [27], as provided by suppliers. This approach allowed to keep a constant composition of the surrogate fuel mixture used in the simulations, avoiding the need of varying any other parameter in order to match the experimental measurements.

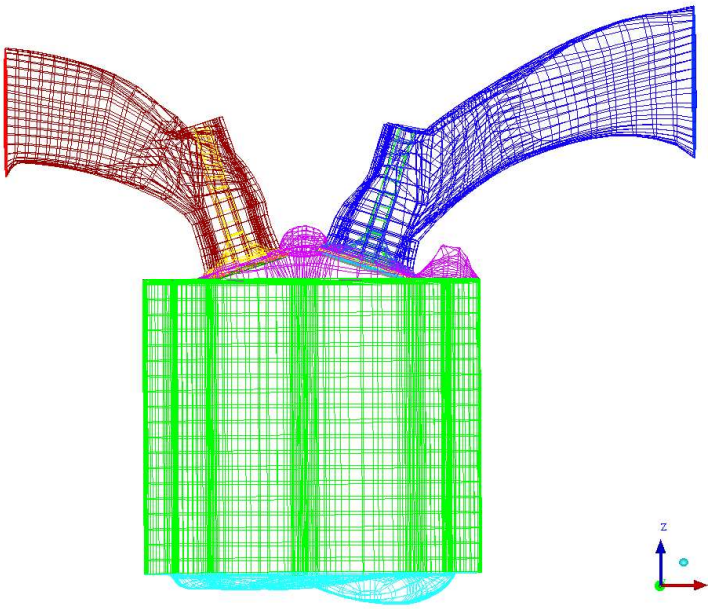

Figure 3: Computational mesh of the SI engine used in the experiments [27] with pent-roof and flat-top piston, 100,000 cells at BDC including intake and exhaust valves.

3 Numerical setup

Figure 3 shows the 3D computational mesh of the engine whose specifications are reported in Table 3.

A fully structured computational mesh, containing around 100,000 cells at Bottom Dead Center (BDC), including the intake and exhaust manifolds, was employed in the present study. Considering that about 20% of the total number of cells was used for the manifolds, it results that the mesh density within the cylinder was about 320 $cells/cm^3$, with the majority of the cells located near the cylinder head and the bowl piston. This value was selected in accordance to the studies in which the main sub-models used in this work were validated, as well as, on the basis of the values adopted in previous studies based on the same version of the KIVA code.

In the work by Vishwanathan et al. [56], a mesh density within the cylinder of 80 $cells/cm^3$, was sufficient for validating the soot model and obtaining good agreement

Table 3: Engine specifications.

Name	**Units**	**Value**
Cylinder volume	cm^3	250
Bore	mm	72
Stroke	mm	60
Compression ratio	None	10.5
Max power	kW	16 at 8000 rpm
Max torque	Nm	20 at 5500 rpm

Table 4: Operating condition specifications.

Engine speed [rpm]	**O_2 [%vol]**	**Spark Advance [CAD ATDC]**
2000	0	-22.0
	5	-12.5
	10	-12.5
4000	0	-24.0
	5	-24.0
	10	-24.0

with the experiments. Liang et al. [81], in the work in which the G-equation model was coupled with detailed chemical kinetics, performed a successfully validation with a mesh density within the cylinder of about 200 $cells/cm^3$. Singh et al. [82] used the combustion model developed by Liang et al. [68, 81] to simulate the combustion in a dual-fuel engine. In that study, a mesh density within the cylinder of about 40 $cells/cm^3$, ensured good results. Furthermore, the same version of the code used in the present study, was recently used in two works carried out by Jiao and Reitz [57, 58]. In both studies, a mesh density within the cylinder of about 90 $cells/cm^3$ produced more than satisfactory results. In all the considered case, a fully structured meshes was employed, as well.

On the basis of the analyzed cases, the mesh density value selected for the present study can be considered adequate, being it abundantly larger than those used in each of the above-mentioned works and the cells distribution comparable.

The initial in-cylinder mixture was assumed to be completely homogeneous, and the simulations started from intake valve closure (IVC). A value of 2.0 for the only model constant C_{m} that needed to be tuned was found to give the best results for the considered SI engine. It was kept constant for all the cases considered in this work.

In the experiments [27], 5% and 10% by volume of additional oxygen was mixed with gasoline within the intake manifold to explore loads higher than the wide open throttle case. All the tests were performed at steady state conditions and two engine speeds were investigated, namely 2000 and 4000 rpm. The list of the conditions and important engine settings considered in the tests are reported in Table 4. At 2000 rpm it was necessary reducing the spark-advance with oxygen addition, in order to avoid the onset of knocking phenomena in the experiments [27].

In-cylinder pressure and HRR traces obtained from the simulations were compared with the experimental measurements in order to validate the numerical results. Then the results were further analyzed to provide in-cylinder soot distributions and to better understand the reasons for the experimentally observed soot particle size distributions.

4 Results and discussion

Before simulating the considered fired cycles, a simulation without combustion was performed, in order to match experimental motored pressure traces and thus verify the information related to the compression ratio. The only available motored in-cylinder pressure trace was recorded at 2000 rpm. No data were available at 4000 rpm in this condition. Therefore, a simulation was performed at 2000 rpm, considering a compression ratio equal to 10.5, in accordance with the information provided in the experimental work by Catapano et al. [27], on which this study is based (cf. Table 3). The results are reported in Figure 4.

Figure 5 reports the in-cylinder pressure and HRR for the two engine speeds considered and illustrates that the effect of oxygen addition was to speed up the combustion process. At 4000 rpm the effects are more evident since these cases have similar combustion phasing (as previously mentioned, at 2000 rpm, it was necessary to delay the ignition timing to avoid knock). The faster combustion is ascribable to the higher burning velocity due to oxygen addition [24]. The lower N_2 content (which is an inert that lowers the flame temperature by absorbing heat without actively participating to the combustion), results in a higher local oxygen availability, contributing to the formation of a more homogeneous mixture that enhances the ignition as well as the flame propagation process.

The lower in-cylinder pressures obtained with 5% of additional oxygen at 2000 rpm, in comparison to the baseline case, are uniquely due to the spark-advance reduction by 9.5 CAD operated in the experiments to avoid knock (as reported in the work by Catapano et al. [27]) when oxygen was added at low speed (cf. Table 4). The spark-advance was kept constant when the amount of additional oxygen was increased from 5 to 10% by volume, for both the engine speeds. As a result, the in-cylinder pressure traces with 10% of additional oxygen resulted higher than those recorded with 5% of oxygen, at both low and high engine speeds, confirming that the in-cylinder

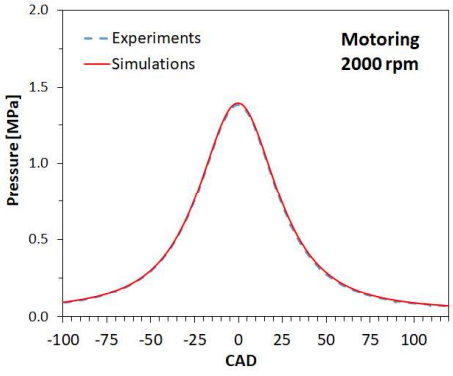

Figure 4: In-cylinder pressure trace during motoring conditions at 2000 rpm. Dashed lines: experiments [27]; solid lines: simulations.

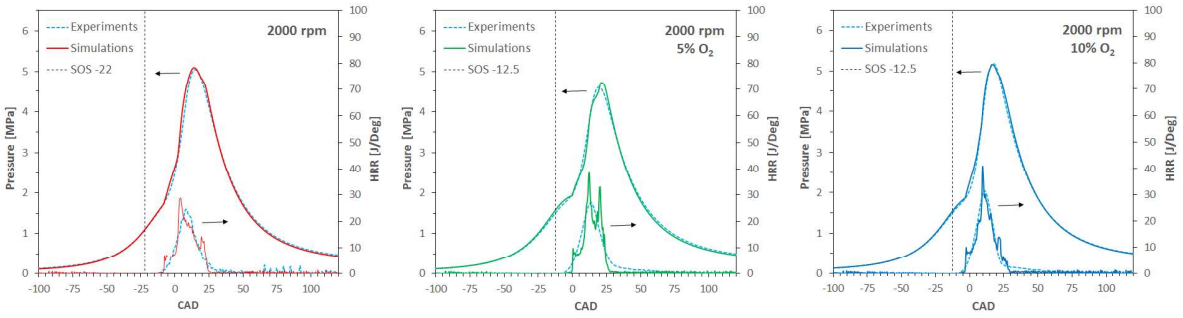

(a) 2000 rpm

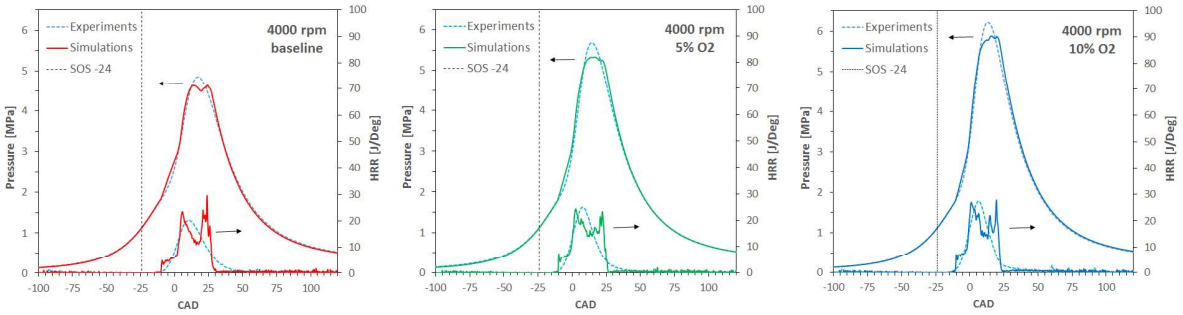

(b) 4000 rpm

Figure 5: In-cylinder pressure and HRR traces at 2000 (a) and 4000 (b) rpm. Dashed lines: experiments [27]; solid lines: simulations; vertical dashed lines: Spark Advance.

pressure reduction with 5% of additional oxygen with respect to the baseline case at 2000 rpm, can be uniquely ascribable to the spark-advance reduction performed in the experiments by Catapano et al. [27].

The above described trends are faithfully replicated by the simulations when the spark-advance and the additional oxygen amount are changed accordingly to the experimental tests. The comparison between the numerical simulations and the experiments is reported in Figure 5, as well. The overall results can be considered more than satisfactory. Very good agreement was obtained for the low speed case (Figure 5a), while some slight discrepancies were found for the high speed case (Figure 5b). These can be probably attributed to the absence of a crevice model.

In general, the absence of a crevice model results in an overestimation of the predicted in-cylinder pressure, as observed in many studies that compared measured in-cylinder pressure traces with those calculated without any crevice model, during motoring conditions [83, 84]. In light of this result, it is reasonable to suppose that the actual compression ratio in the experiments might have been slightly lower than the declared one (the information provided by engine's manufacturers was not verified in the experimental work [27], since was not crucial in that circumstance).

However, it must also be considered that the engine speed plays a significant role in determining the piston-ring flows. Specifically, the more is the engine speed, the less is the influence of the crevice flow [83, 85]. Rakopoulos et al. [83] observed that

increasing the engine speed during motoring conditions produces a higher increase in the measured in-cylinder pressure than that observed in the simulations without a crevice model. Considering that the numerical results reported in Figure 4 matched the available experimental motored pressure trace at the lowest speed (namely, 2000 rpm), it derives that simulations at higher speeds (such as 4000 rpm) would underestimate the motored pressure peak, once compared with the experiments. When fired conditions are considered, these effects can be more relevant and can reasonably explain why the absence of a crevice model produced an underestimation of the in-cylinder pressure at the higher engine speeds.

The absence of a crevice region can also explain the presence of a second pressure bump after the main peak observed from the baseline case at 4000 rpm (left-hand plot in Figure 5b). In real conditions, a significant amount of unburned gas ahead of the flame flows into the top-land crevice and it has been calculated that the crevice flow reduces the instantaneous in-cylinder charge mass by as much as 6% [86]. About 80% of this trapped mass (about 5% of the total cylinder mass) eventually returns to the chamber and is burned during the later stages of combustion, when the temperature is much lower [86]. In the simulations, the absence of this zone (i.e., a model that simulates this phenomenon) has the result that all the in-cylinder fuel survives far the flame propagation and is oxidized at higher temperatures, resulting in a sudden increase of pressure and a faster HRR at the conclusion of the combustion phase. At lower speeds this behavior is less relevant and therefore the simulations show better agreement.

Figure 6 points out that for all conditions the effect of oxygen addition is to increase the IMEP. The increment is almost linear, namely adding 10% of oxygen results in a load increase of roughly 10% and this trend is well captured by the numerical model, especially for the low speed conditions. At 4000 rpm the IMEP increase is slightly overestimated due to the above-described crevice flow reasons. It must be noticed that stoichiometric conditions were kept during the experimental tests and therefore the

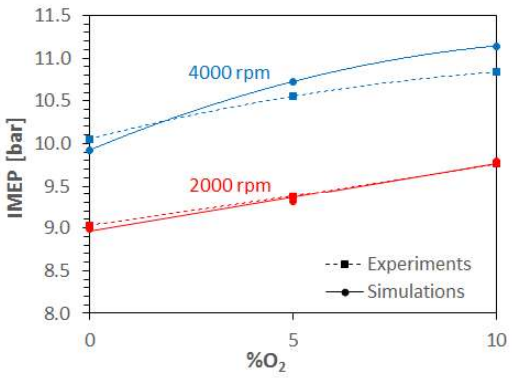

Figure 6: Load increase due to oxygen addition. Dashed lines: experiments [27]; solid lines: simulations.

increased IMEP values are ascribed to the larger amount of fuel that was injected, as is inferable from the larger fuel consumption that was recorded for the cases with oxygen addition.

The numerical model can be considered to have been successfully validated against the experimental data and can be used for a deeper analysis of the results relating to particle emission processes. In particular, the low-speed case, which showed the best agreement, was chosen for further investigation on the combustion and soot formation processes that are taking place within the engine. For sake of brevity, the two extreme cases, namely 0 and 10% of oxygen, are compared.

Figure 7 illustrates the propagation of the flame front location as represented by the G=0 (pink) surface after the transition from the kernel growth model to the turbulent flame propagation model, as well as the temperature distributions (cross section on x-z plane). The red particles in the center were used to represent the kernel surface. The results indicate that combustion is due to flame propagation and that no auto-ignition (knock) is observed. The burnt regions swept by the flame surface can be easily distinguished from the unburnt regions.

The spark advance was delayed to avoid knock (Table 4) and therefore the turbulent flame with 10% oxygen (right-hand side of Figure 7) starts to propagate later than the baseline case. In the latter case, at -5°ATDC the transition from kernel growth to flame propagation has already occurred, while in the higher-load case the kernel is still growing. At TDC, in both cases, the turbulent flame is completely formed and it propagates radially towards the cylinder walls with a quasi-spherical shape. The fastest flame speed was found with oxygen addition, as can be inferred from the fact that at 10° ATDC the flame front position is practically the same, even though the spark was triggered 9 CAD later in the oxygen-enriched case. The two flames reach the cylinder wall simultaneously at about 20° ATDC. Slightly higher temperatures in the burned region are reached in a shorter time with oxygen addition, and in both cases the lowest temperature is recorded near the spark-plug location, due to the particular cylinder-head shape.

The average in-cylinder temperature evolution is reported in Figure 8(b), which summarizes the results discussed in the previous figures and allows a comparison with the average in-cylinder pressure and HRR traces (Figure 8(a)). Figure 8(c) shows the time evolution of the soot mass per kg of fuel. When combustion begins, soot starts to increase and the highest peak is recorded in correspondence with the higher in-cylinder pressures and temperatures, just before the front flame reaches the wall. After that, soot decreases and oxygen addition produces a lower specific value of soot mass at EVO.

In the next six figures the distributions of six variables of interest, i.e., mass fractions of OH, C_2H_2, A_4, and soot, soot number density (PN) and particle size (D_p) are reported to analyze the causes of the observed soot emission trends.

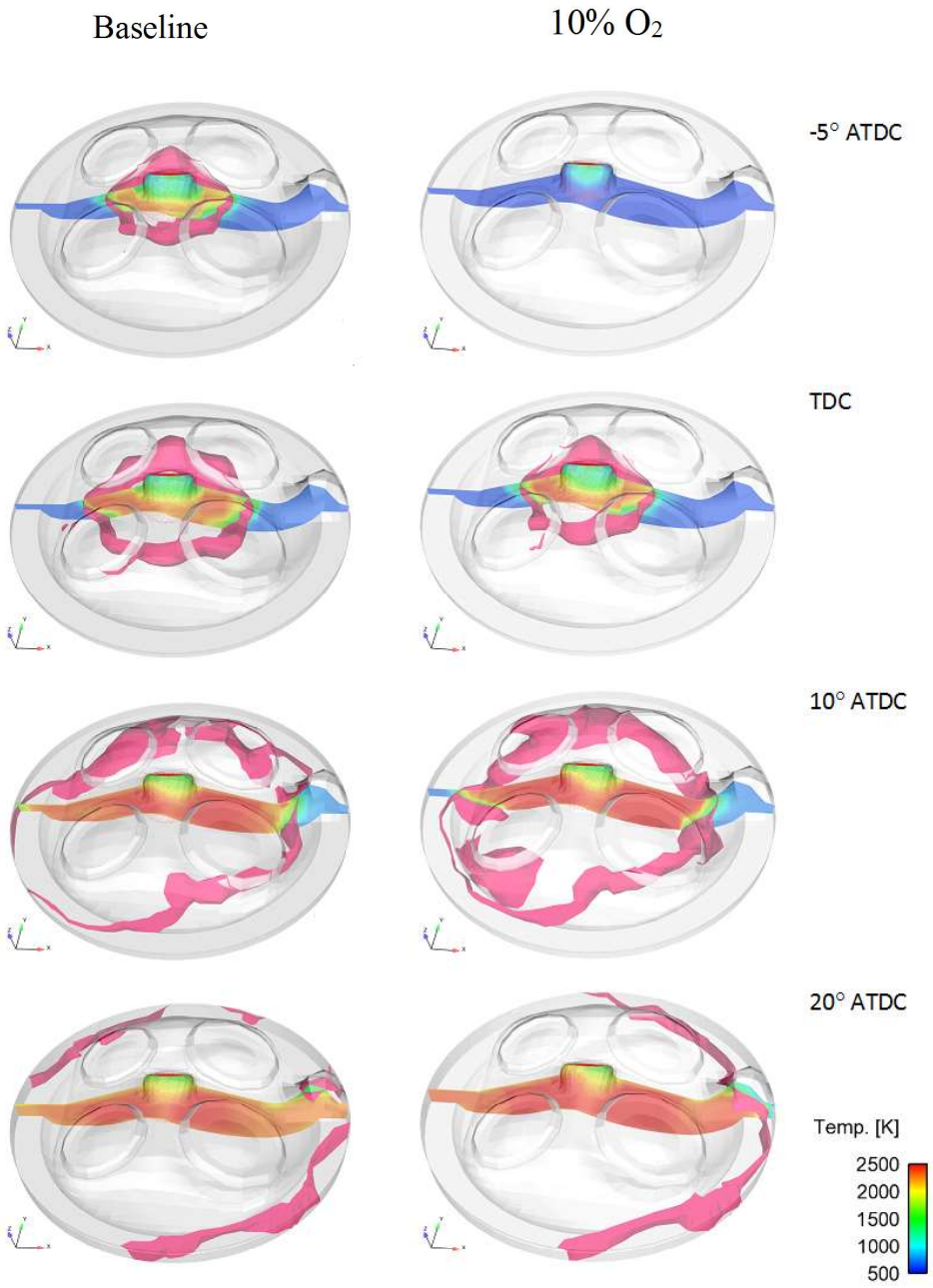

Figure 7: Evolution of in-cylinder turbulent flame and temperature field (plane x-z) for 2000 rpm case in the simulations. Red particles: kernel surface; pink surface: flame front.

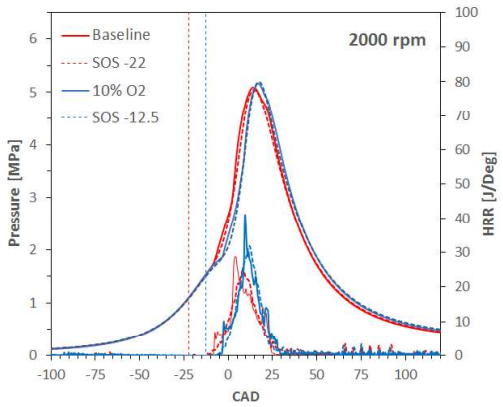

(a)

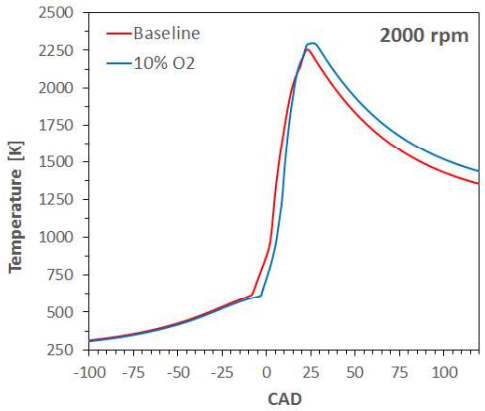

(b)

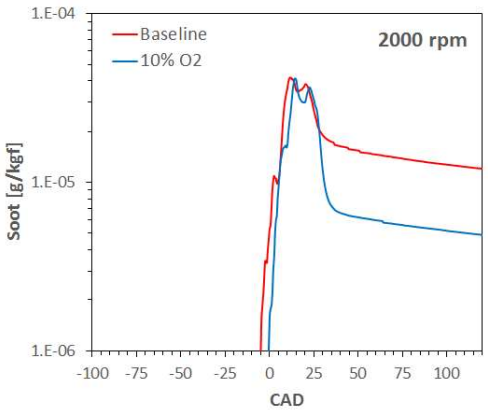

(c)

Figure 8: In-cylinder time evolution of pressure and HRR traces (a). Temperature (b) and specific soot mass (c) in the simulations of the 2000 rpm cases. Dashed lines: experiments [27]; solid lines: simulations; vertical dashed lines: Spark Advance.

Figure 9 shows that the in-cylinder OH concentration increases in the region behind the front flame and then start to decrease once the flame has reached the wall and the temperatures are falling. In the central region, near the spark-plug location, low OH concentration levels can be observed during the entire combustion process. At 20° ATDC, when the flame has reached the in-cylinder wall, the OH concentration is larger for the high-load case of 10% of oxygen.

The OH concentration is crucial for the soot oxidation process, while soot inception and surface growth depend on the in-cylinder concentration and distribution of the soot precursors. In Figure 10 and Figure 11 is therefore reported the time evolution of the mass fraction distributions of C_2H_2 and A_4, respectively, which are the most abundant gaseous hydrocarbon species detectable in regions where soot is formed. The highest values of their concentrations are recorded in the burned region, near the flame front and where the temperatures are lower, namely near the spark-plug location, in both cases. The mass fraction of these two species decreases after the flame, which is responsible for their production, reaches the cylinder wall and sufficient residence time at high temperatures is available in regions rich of OH radicals. In fact, at exhaust valve opening time (120° ATDC) these precursor species are mainly found near the center of the cylinder head due to the lack of OH radicals and the lower temperatures (Figure 10(c) and Figure 11(c)). With oxygen addition, a slightly larger amount of C_2H_2 and A_4 can be detected.

A competition between the increased concentration of species responsible for soot generation and, at the same time, of OH radicals, which contribute to its oxidation, explains the time evolution of the soot mass fraction reported in Figure 12. In other words, higher soot mass fractions are seen near the fame front regions, where the in-cylinder temperatures are higher and there is abundance of C_2H_2 and A_4, while in the burnt regions, the oxidation process by OH radicals starts to take place, and thus the soot mass fraction is reduced (Figure 12(a) and Figure 12(b)). Oxygen addition enhances this aspect, increasing the production rates of both OH radicals and soot precursor species and therefore, at 120° ATDC, the in-cylinder soot mass distribution obtained with oxygen addition is comparable to the baseline case. Since stoichiometric conditions were considered in both cases the soot mass per kg of fuel is lower for the oxygenated combustion case, as previously shown in Figure 8(c).

From Figure 13 and Figure 14 it is also possible to observe that at TDC, soot particles with larger sizes are located near the flame front (Figure 14(a)), where the C_2H_2 and A_4 concentrations are higher, but the highest number density levels are recored near the spark-plug location (Figure 13(a)), where the temperatures are not high enough for a fast soot inception and growth process. At 120° ATDC the largest part of the formed soot is composed of very fine particles.

These results are in perfect agreement with the experimental measured PSDs, shown

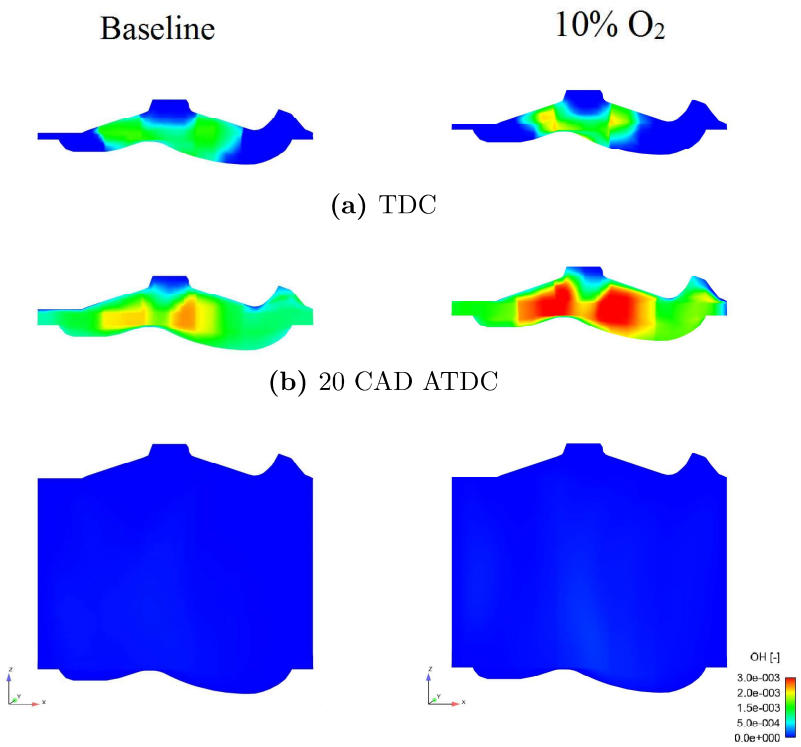

(a) TDC

(b) 20 CAD ATDC

(c) 120 CAD ATDC

Figure 9: Time evolution of mass fraction distribution of OH radicals.

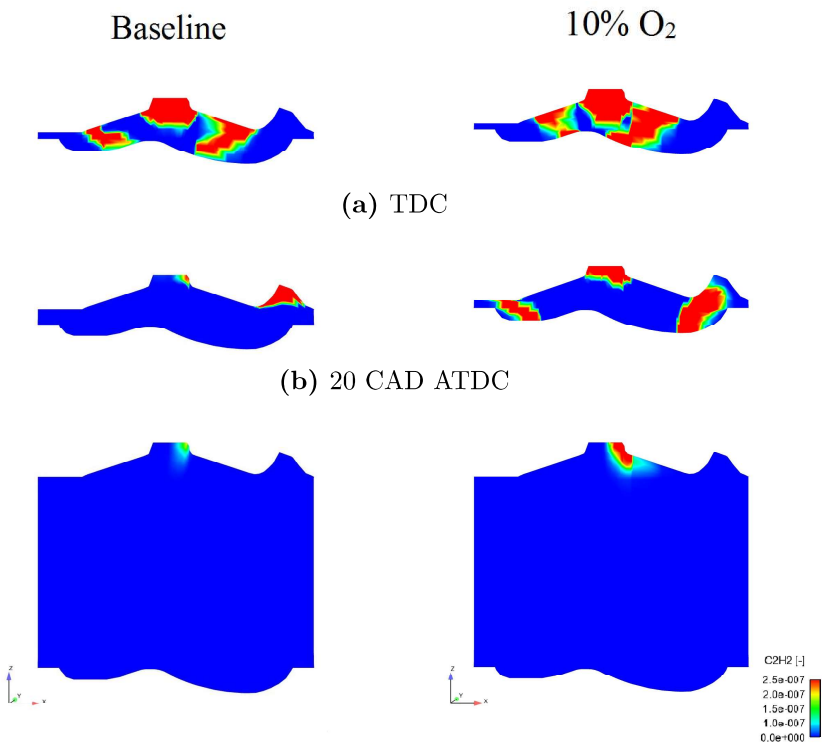

(a) TDC

(b) 20 CAD ATDC

(c) 120 CAD ATDC

Figure 10: Time evolution of mass fraction distribution of C_2H_2.

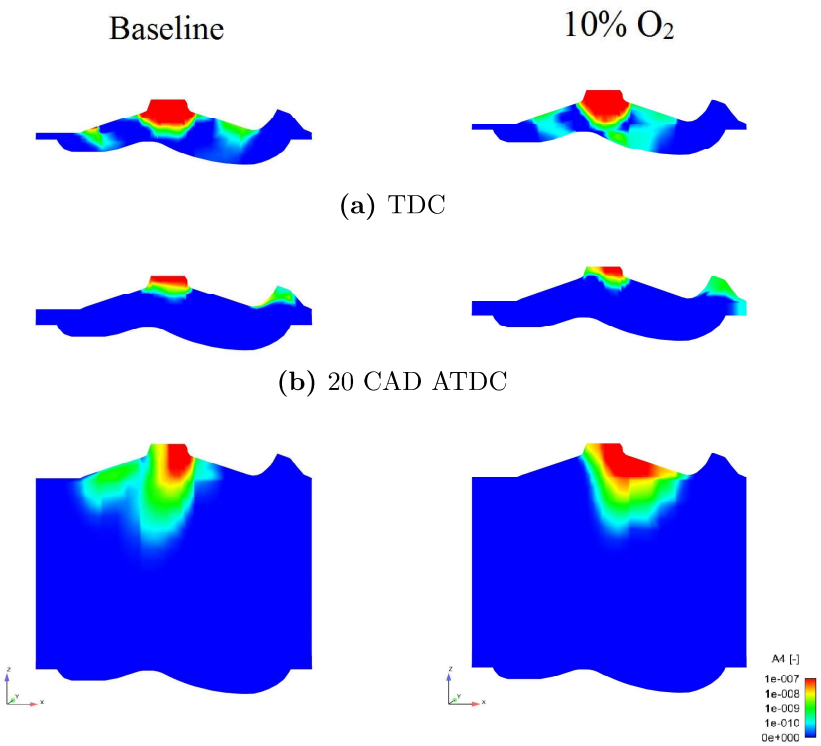

(a) TDC

(b) 20 CAD ATDC

(c) 120 CAD ATDC

Figure 11: Time evolution of mass fraction distribution of A_4.

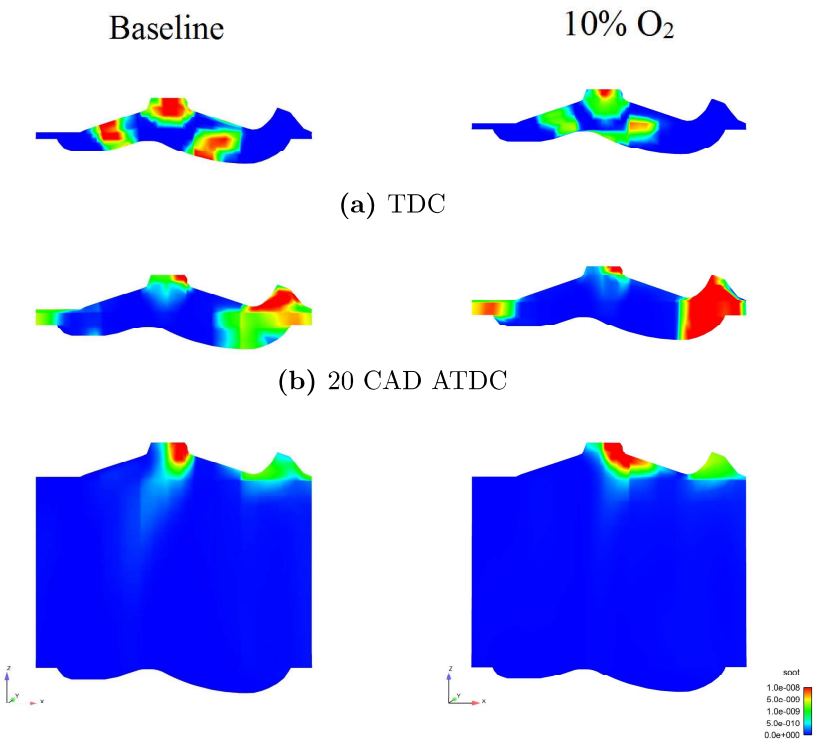

(a) TDC

(b) 20 CAD ATDC

(c) 120 CAD ATDC

Figure 12: Time evolution of soot mass fraction distribution .

(a) TDC

(b) 20 CAD ATDC

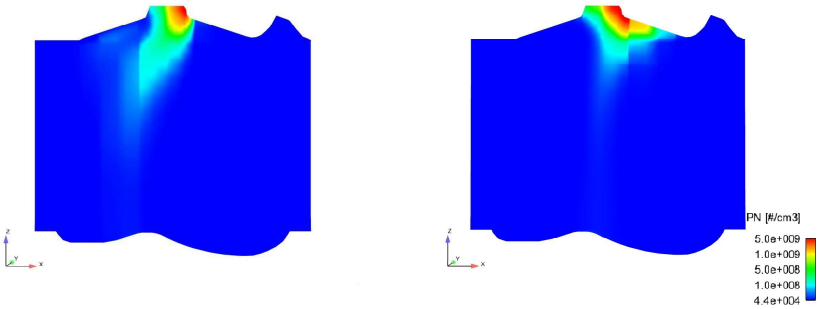

(c) 120 CAD ATDC

Figure 13: Time evolution of soot number density distribution.

(a) TDC

(b) 20 CAD ATDC

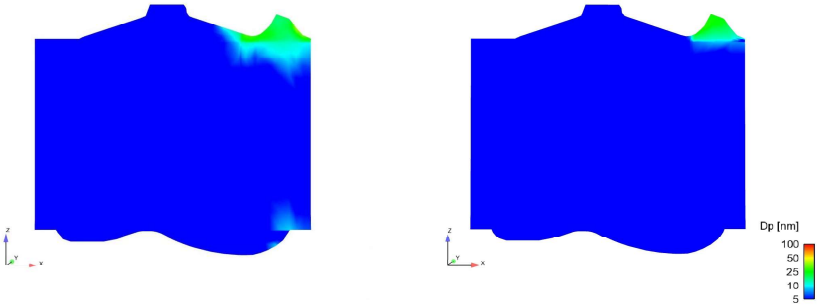

(c) 120 CAD ATDC

Figure 14: Time evolution of soot particle sizes distribution.

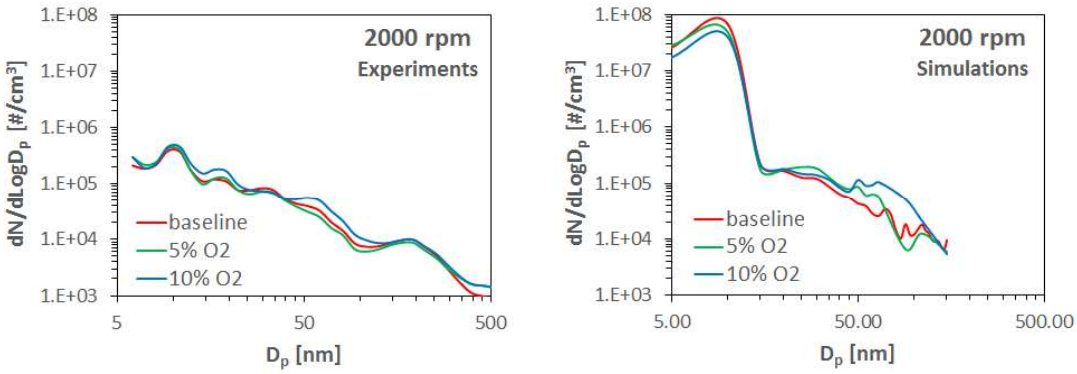

(a) (b)

Figure 15: Experimental [27] (a) and predicted (a) PSD functions.

in Figure 15(a) and which pointed out that the load increase obtained by oxygen addition did not affect the granulometric distribution of the particles emitted from the engine at 2000 rpm. Computed PSDs are reported in Figure 15(a). The agreement with the experiments can be considered to be very good for particles with sizes larger than 15 nm. The number of the finest particles is overestimated by the numerical model, but it must be considered that oxidation, which could occur in the exhaust, as well as physical soot transformation, i.e., due to the discharge process of the gasses from the combustion chamber into the exhaust pipe, or due to temperature conditions changing along the exhaust line or within the instrument can have strong effect on nucleation mode particles. This may explain the lower value detected by the particle sampler device within the exhaust pipe [2].

5 Conclusions

The present study analyzed the effect of a load increase on gasoline SI engine combustion, by means pure oxygen addition. 3-D Computational Fluid Dynamics simulations were performed and the numerical results were compared with existing experimental data, in which 5 and 10% by volume of additional oxygen was inducted with gasoline within the intake manifold of a SI engine to explore loads higher than the wide open throttle case. All the tests were performed at stoichiometric and steady state conditions and two engine speeds were investigated, namely 2000 and 4000 rpm. Such an approach provides additional basic information about oxygenated fuels and combustion, while avoiding still existing uncertainties relating to chemistry models.

The effect of oxygen addition was to speed up the combustion process and the induced increase in load was roughly linear with increased oxygen content. At 4000 rpm the effects were more evident than at 2000 rpm, because in the latter case it was necessary to delay the ignition timing to avoid knock in the experiments. Very good agreement was obtained for the low speed case, while some discrepancies, which are

attributed to the absence of a crevice model, were found for the high speed case.

Further investigation on the combustion and soot formation processes was provided at 2000 rpm. Oxygen addition produced a faster burning velocity and higher in-cylinder temperatures. During the initial combustion stages, higher soot mass fractions were seen near the fame front regions, where the in-cylinder temperatures were higher and there was abundance of C_2H_2 and A_4. Afterwards, the oxidation process by OH radicals started to take place, and thus the soot mass fraction was reduced. At EVO (120° ATDC) soot was mainly found in the center of the cylinder head due to the lack of OH radicals and the lower temperatures that characterized this region. Oxygen addition enhanced this aspect, increasing the production rates of both OH radicals and soot precursor species and therefore, at 120° ATDC, the in-cylinder soot mass distribution obtained with oxygen addition was comparable to the baseline case. However, since stoichiometric conditions were considered in both cases the soot mass per kg of fuel was lower for the oxygenated combustion case.

The results were in good agreement with experimentally measured PSDs and provide confidence in the soot model in predicting soot emissions. In addition, the comparison between measured and predicted PSDs showed very good agreement for particles with sizes larger than 15 nm, but the number of the finest particles was overestimated by the numerical model. This can be explained by considering oxidation process occurring in the exhaust,which was not considered in the simulations.

References

[1] Bischof, O. F. *Recent Developments in the Measurement of Low Particulate Emissions from Mobile Sources: A Review of Particle Number Legislations. Emission Control Science and Technology*, 2015. volume 1(2):203–212.

[2] Amirante, R., Distaso, E., Tamburrano, P., and Reitz, R. D. *Measured and Predicted Soot Particle Emissions from Natural Gas Engines. SAE Tech Pap 2015-24-2518*, 2015. doi:doi:10.4271/2015-24-2518.

[3] Andersson, J., Mamakos, A., Giechaskiel, B., Carriero, M., and Martini, G. *Particle Measurement Programme (PMP) heavy-duty inter-laboratory correlation exercise (ILCE_HD) final report. Final Report. Joint Research Center, Ispra (VA). EUR*, 2010. volume 24561.

[4] Amirante, R., Distaso, E., Napolitano, M., Tamburrano, P., Iorio, S., Sementa, P., Vaglieco, B., and Reitz, R. *Effects of lubricant oil on particulate emissions from port-fuel and direct-injection spark-ignition engines. International Journal of Engine Research*, 2017. volume 18(5-6):606—-620. doi:10.1177/1468087417706602.

[5] Coulier, J. *Using Alcohol Fuels in Dual Fuel Operation of Compression Ignition Engines : A Review. 28th CIMAC World Congress*, 2016.

[6] Asad, U., Kumar, R., Zheng, M., and Tjong, J. *Ethanol-fueled low temperature combustion: A pathway to clean and efficient diesel engine cycles. Applied Energy*, 2015. volume 157:838–850.

[7] Nishi, M., Kanehara, M., and Iida, N. *Assessment for innovative combustion on HCCI engine by controlling EGR ratio and engine speed. Applied Thermal Engineering*, 2016. volume 99:42–60.

[8] Patil, M. D. A. and Patil, R. Y. *A Review Latest Emission Control Techniques in Internal Combustion Engine. Journal of Mechanical and Mechanics Engineering*, 2016. volume 2(3):12–27.

[9] Amirante, R., Casavola, C., Distaso, E., and Tamburrano, P. *Towards the Development of the In-Cylinder Pressure Measurement Based on the Strain Gauge Technique for Internal Combustion Engines. SAE Technical Paper 2015-24-2419*, 2015.

[10] Amirante, R., Coratella, C., Distaso, E., Rossini, G., and Tamburrano, P. *Optical device for measuring the injectors opening in common rail systems. International Journal of Automotive Technology*, 2017. volume 18(4):729—-742.

[11] Wang, J. and Wang, Z. *Research progress of high efficient and clean combustion of automotive gasoline engines. Journal of Automotive Safety and Energy*, 2010. volume 3:4.

[12] Wang, Z., Liu, H., and Reitz, R. D. *Knocking combustion in spark-ignition engines. Progress in Energy and Combustion Science*, 2017. volume 61:78–112.

[13] Yi, J., Wooldridge, S., Coulson, G., Hilditch, J., Iyer, C. O., Moilanen, P., Papaioannou, G., Reiche, D., Shelby, M., VanDerWege, B., and Others. *Development and optimization of the Ford 3.5 L V6 EcoBoost combustion system. SAE International Journal of Engines*, 2009. volume 2(1):1388–1407.

[14] Distaso, E., Amirante, R., Calò, G., De Palma, P., Tamburrano, P., and Reitz, R. D. *Investigation of Lubricant Oil influence on Ignition of Gasoline-like Fuels by a Detailed Reaction Mechanism. Energy Procedia*, 2018. volume 148:663–670.

[15] Zhao, F., Lai, M.-C., and Harrington, D. L. *Automotive spark-ignited direct-injection gasoline engines. Progress in energy and combustion science*, 1999. volume 25(5):437–562.

[16] Willand, J., Daniel, M., Montefrancesco, E., Geringer, B., Hofmann, P., and Kieberger, M. *Limits on downsizing in spark ignition engines due to pre-ignition. MTZ worldwide*, 2009. volume 70(5):56–61.

[17] Winklhofer, E., Hirsch, A., Kapus, P., Kortschak, M., and Philipp, H. *TC GDI engines at very high power density—irregular combustion and thermal risk.* Technical report, SAE Technical Paper, 2009.

[18] Inoue, T., Inoue, Y., and Ishikawa, M. *Abnormal combustion in a highly boosted SI engine-the occurrence of super knock.* Technical report, SAE Technical Paper, 2012.

[19] Dahnz, C. and Spicher, U. *Irregular combustion in supercharged spark ignition engines–pre-ignition and other phenomena. International Journal of Engine Research*, 2010. volume 11(6):485–498.

[20] Kalghatgi, G. T. and Bradley, D. *Pre-ignition and 'super-knock'in turbo-charged spark-ignition engines. International Journal of Engine Research*, 2012. volume 13(4):399–414.

[21] Amann, M., Mehta, D., and Alger, T. *Engine operating condition and gasoline fuel composition effects on low-speed pre-ignition in high-performance spark ignited gasoline engines. SAE International Journal of Engines*, 2011. volume 4(2011-01-0342):274–285.

[22] Zaccardi, J.-M. and Escudié, D. *Overview of the main mechanisms triggering low-speed pre-ignition in spark-ignition engines. International Journal of Engine Research*, 2015. volume 16(2):152–165.

[23] Zhuang, H., Hung, D., Xu, M., Chen, H., Li, T., Zhang, Y., Yang, J., and Men, Y. *Flame area correlations with heat release at early flame development of combustion process in a spark-ignition direct-injection engine using gasoline, ethanol and butanol. SAE Technical Papers*, 2013. volume 11.

[24] Zhou, J., Richard, S., Mounaim-Rousselle, C., and Foucher, F. *Effects of Controlling Oxygen Concentration on the Performance, Emission and Combustion Characteristics in a Downsized SI Engine. SAE Tech Paper 2013-24-0056*, 2013. (2013-24-0056).

[25] Caton, J. A. *Use of a cycle simulation incorporating the second law of thermodynamics: results for spark-ignition engines using oxygen enriched combustion air.* Technical report, SAE Technical Paper, 2005.

[26] Wu, Y.-Y. and Huang, K. D. *Improving the performance of a small spark-ignition engine by using oxygen-enriched intake air.* Technical report, SAE Technical Paper, 2007.

[27] Catapano, F., Iorio, S. D., Luise, L., Sementa, P., and Vaglieco, B. M. *Experimental Analysis of O 2 Addition on Engine Performance and Exhaust Emissions from a Small Displacement SI Engine. SAE Tech Paper No. 2016-01-0697*, 2016. pp. 2–7.

[28] Han, B.-Y., Bei, S.-Y., Wang, X.-M., Yao, J.-K., Fan, X., and Hang, W.-X. *The effect on gasoline engine emission characteristics of variable composition oxygen-enriched intake air systems and analysis of heat-resistant and anti-corrosion coatings with remanufacturing. The Open Fuels & Energy Science Journal*, 2015. volume 8(1).

[29] Bing-Yuan, H., Shao-Yi, B., Xiu-Qing, X., Hong-Liang, L., and Jiang-Wei, C. *Research on control strategy of oxygen-rich intake based on map of gasoline engine. Sensors & Transducers*, 2013. volume 161(12):530.

[30] Gao, Q., LIU, C.-c., JIN, Y.-a., MA, C.-q., ZHANG, G.-j., and SU, J.-l. *Investigation on start emission and misfire characteristics of spark ignition engine intaking oxygen-enriched air [j]. Chinese Internal Combustion Engine Engineering*, 2010. volume 3:003.

[31] Zhou, J., Cordier, M., Mounaïm-Rousselle, C., and Foucher, F. *Experimental estimate of the laminar burning velocity of iso-octane in oxygen-enriched and co2-diluted air. Combustion and Flame*, 2011. volume 158(12):2375–2383.

[32] Amirante, R., Distaso, E., Di Iorio, S., Sementa, P., Tamburrano, P., Vaglieco, B. M., and Reitz, R. D. *Effects of Natural Gas Composition on Performance and Regulated, Greenhouse Gas and Particulate Emissions in Spark-Ignition Engines. Energy Conversion and Management*, 2017. volume 143:338–347.

[33] Distaso, E., Amirante, R., Tamburrano, P., and Reitz, R. D. *Steady-state Characterization of Particle Number Emissions from a Heavy-Duty Euro VI Engine Fueled with Compressed Natural Gas. Energy Procedia*, 2018. volume 148:671–678.

[34] Gao, D., Jin, Z., Zhang, J., Li, J., and Ouyang, M. *Development and performance analysis of a hybrid fuel cell/battery bus with an axle integrated electric motor drive system. International Journal of Hydrogen Energy*, 2016. volume 41(2):1161–1169.

[35] Alaswad, A., Baroutaji, A., and Olabi, A. G. *Application of Fuel Cell Technologies in the Transport Sector. Current Challenges and Developments. State of the Art on Energy Developments*, 2015. volume 11:251.

[36] Amirante, R., Distaso, E., Tamburrano, P., and Reitz, R. D. *Analytical Correlations for Modeling the Laminar Flame Speed of Natural Gas Surrogate Mixtures. Energy Procedia*, 2017. volume 126:850–857.

[37] Lave, L. B. and Maclean, H. L. *An environmental-economic evaluation of hybrid electric vehicles : Toyota's Prius vs its conventional internal combustion engine Corolla. Transportation Research Part D: Transport and Environment*, 2002. volume 7(2):155–162.

[38] Balki, M. K., Sayin, C., and Canakci, M. *The effect of different alcohol fuels on the performance, emission and combustion characteristics of a gasoline engine. Fuel*, 2014. volume 115:901–906.

[39] Catapano, F., Di Iorio, S., Magno, A., Sementa, P., and Vaglieco, B. M. *A comprehensive analysis of the effect of ethanol, methane and methane-hydrogen blend on the combustion process in a PFI (port fuel injection) engine. Energy*, 2015. volume 88:101–110.

[40] Kim, N., Cho, S., and Min, K. *A study on the combustion and emission characteristics of an SI engine under full load conditions with ethanol port injection and gasoline direct injection. Fuel*, 2015. volume 158:725–732.

[41] Masum, B. M., Masjuki, H. H., Kalam, M. A., Fattah, I. M. R., Palash, S. M., and Abedin, M. J. *Effect of ethanol–gasoline blend on NOx emission in SI engine. Renewable and Sustainable Energy Reviews*, 2013. volume 24:209–222.

[42] Nadim, F., Zack, P., Hoag, G. E., and Liu, S. *United States experience with gasoline additives. Energy Policy*, 2000. volume 29(1):1–5. ISSN 03014215. doi: 10.1016/S0301-4215(00)00099-9.

[43] Yunoki, S. and Saito, M. *A simple method to determine bioethanol content in gasoline using two-step extraction and liquid scintillation counting. Bioresource technology*, 2009. volume 100(23):6125–6128.

[44] Tran, L. S., Sirjean, B., Glaude, P.-A., Fournet, R., and Battin-Leclerc, F. *Progress in detailed kinetic modeling of the combustion of oxygenated components of biofuels. Energy*, 2012. volume 43(1):4–18.

[45] Fisher, E. M., Pitz, W. J., Curran, H. J., and Westbrook, C. K. *Detailed chemical kinetic mechanisms for combustion of oxygenated fuels. Proceedings of the combustion institute*, 2000. volume 28(2):1579–1586.

[46] Ogawa, H., Miyamoto, N., and Yagi, M. *Chemical-kinetic analysis on PAH formation mechanisms of oxygenated fuels. SAE Technical Paper*, 2003. (2003-01-3190). doi:10.4271/2003-01-3190.

[47] Harper, M. R., Van Geem, K. M., Pyl, S. P., Marin, G. B., and Green, W. H. *Comprehensive reaction mechanism for n-butanol pyrolysis and combustion. Combustion and Flame*, 2011. volume 158(1):16–41.

[48] Herbinet, O., Biet, J., Hakka, M. H., Warth, V., Glaude, P.-A., Nicolle, A., and Battin-Leclerc, F. *Modeling study of the low-temperature oxidation of large methyl esters from C 11 to C 19. Proceedings of the Combustion Institute*, 2011. volume 33(1):391–398.

[49] Gallo, Y., Li, Z., Richter, M., and Andersson, O. *Parameters influencing soot oxidation rates in an optical diesel engine. SAE International Journal of Engines*, 2016. volume 9(4):2044–2055.

[50] Angrill, O., Geitlinger, H., Streibel, T., Suntz, R., and Bockhorn, H. *Influence of exhaust gas recirculation on soot formation in diffusion flames. Proceedings of the combustion Institute*, 2000. volume 28(2):2643–2649.

[51] Lopez, J. J., Martin, J., Garcia, A., Villalta, D., Warey, A., and Domenech, V. *Characterization of in-cylinder soot oxidation using two-color pyrometry in a production light-duty diesel engine.* Technical report, SAE Technical Paper, 2016.

[52] Payri, F., Benajes, J., Novella, R., and Kolodziej, C. *Effect of intake oxygen concentration on particle size distribution measurements from diesel low temperature combustion. SAE International Journal of Engines*, 2011. volume 4(1):1888–1902.

[53] Lequien, G., Andersson, Ö., Tunestal, P., and Lewander, M. *A correlation analysis of the roles of soot formation and oxidation in a heavy-duty diesel engine.* Technical report, SAE Technical Paper, 2013.

[54] Glassman, I. *Soot formation in combustion processes.* In *Symposium (international) on combustion*, volume 22. Elsevier, 1989 pp. 295–311.

[55] Perini, F., Galligani, E., and Reitz, R. D. *An analytical Jacobian approach to sparse reaction kinetics for computationally efficient combustion modeling with large reaction mechanisms. Energy and Fuels*, 2012. volume 26(8):4804–4822. ISSN 08870624. doi:10.1021/ef300747n.

[56] Vishwanathan, G. and Reitz, R. D. *Development of a Practical Soot Modeling Approach and Its Application to Low-Temperature Diesel Combustion. Combustion Science and Technology*, 2010. volume 182(8):1050–1082.

[57] Jiao, Q. and Reitz, R. *Modeling of equivalence ratio effects on particulate formation in a spark-ignition engine under premixed conditions. SAE 2014 World Congress and Exhibition*, 2014. volume 1.

[58] Jiao, Q. and Reitz, R. D. *Modeling soot emissions from wall films in a direct-injection spark-ignition engine. International Journal of Engine Research*, 2014. volume 16(8):994–1013. ISSN 1468-0874.

[59] Fan, L. and Reitz, R. D. *Development of an Ignition and Combustion Model for Spark Ignition Engines. SAE Technical paper*, 2000. (724).

[60] Liang, L. and Reitz, R. D. *Spark Ignition Engine Combustion Modeling Using a Level Set Method with Detailed Chemistry. SAE Paper*, 2006. volume 2006(724).

[61] Tan, Z. and Reitz, R. D. *Modeling Ignition and Combustion in Spark-ignition Engines Using a Level Set Method. SAE Technical Paper 2003-01-0722*, 2003. doi:10.4271/2003-01-0722.

[62] Amirante, R., Distaso, E., Tamburrano, P., and Reitz, R. D. *Laminar Flame Speed Correlations for Methane, Ethane, Propane and their Mixtures, and Natural Gas and Gasoline for Spark-Ignition Engine Simulations. International Journal of Engine Research*, 2017. volume 18(9):951–970.

[63] Amsden, A. A., O'rourke, P. J., and Butler, T. D. *KIVA-II: A computer program for chemically reactive flows with sprays. Los Alamos National Lab., NM (USA)*, 1989. (LA-11560-MS).

[64] Amsden, A. A. and Menon, R. G. *KIVA3. A KIVA Program With Block-Structured Mesh for Complex Geometries. Silicon Graphics Computer Systems, Mountain View, CA (United States)*, 1993. (ESTSC-000154SGSUP00).

[65] Amsden, A. A. *KIVA-3V: A block-structured KIVA program for engines with vertical or canted valves. Los Alamos National Lab., NM (United States)*, 1997. (ESTSC-000154MLTPL01).

[66] Heywood, J. B. and Others. *Internal combustion engine fundamentals*, volume 930. Mcgraw-hill New York, 1988.

[67] Herweg, R. and Maly, R. R. *A fundamental model for flame kernel formation in SI engines. SAE Technical Paper*, 1992. (922243).

[68] Liang, L., Reitz, R. D., Yi, J., and Iyer, C. O. *A G-equation combustion model incorporating detailed chemical kinetics for PFI/DI SI Engine simulations. SAE Congress April*, 2006. volume 2.

[69] Peters, N. *Turbulent combustion*. Cambridge university press, 2000.

[70] Tan, Z. *Multi-dimensional modeling of ignition and combustion in premixed and DIS/CI (direct injection spark/compression ignition) engines*. Doctoral Dissertation, University of Wisconsin–Madison, 2003.

[71] Han, Z., Weaver, C., Wooldridge, S., Alger, T., Hilditch, J., McGee, J., Westrate, B., Xu, Z., Yi, J., Chen, X., and Others. *Development of a new light stratified-charge DISI combustion system for a family of engines with upfront CFD coupling with thermal and optical engine experiments. SAE Technical Paper*, 2004. (2004-01-0545).

[72] Leung, K. M., Lindstedt, R. P., and Jones, W. P. *A simplified reaction mechanism for soot formation in nonpremixed flames. Combustion and flame*, 1991. volume 87(3):289–305.

[73] Hu, E., Li, X., Meng, X., Chen, Y., Cheng, Y., Xie, Y., and Huang, Z. *Laminar flame speeds and ignition delay times of methane-air mixtures at elevated temperatures and pressures. Fuel*, 2015. volume 158:1–10. ISSN 00162361. doi: 10.1016/j.fuel.2015.05.010.

[74] Perini, F., Ra, Y., Hiraoka, K., Nomura, K., Yuuki, A., Oda, Y., Rutland, C., and Reitz, R. *An Efficient Level-Set Flame Propagation Model for Hybrid Unstructured Grids Using the G-Equation. SAE International Journal of Engines*, 2016. volume 9(3):582–2016. ISSN 1946-3944. doi:10.4271/2016-01-0582.

[75] Metghalchi, M. and Keck, J. C. *Burning Velocities of Mixture of Air with Methanol, Iso-Octane and Indolene at High Pressure and Temperature. Combustion and Flame*, 1982. volume 210:191–210.

[76] Gülder, Ö. L. *Correlations of laminar combustion data for alternative SI engine fuels.* Technical report, SAE Technical Paper, 1984.

[77] Sileghem, L., Alekseev, V. A., Vancoillie, J., Van Geem, K. M., Nilsson, E. J. K., Verhelst, S., and Konnov, A. A. *Laminar burning velocity of gasoline and the gasoline surrogate components iso-octane, n-heptane and toluene. Fuel*, 2013. volume 112:355–365. ISSN 00162361. doi:10.1016/j.fuel.2013.05.049.

[78] Zhao, Z., Conley, J. P., Kazakov, a., and Dryer, F. L. *Burning velocities of real gasoline fuel at 353 K and 500 K. SAE-transactions*, 2003. volume 112(724):2624–2629. ISSN 0148-7191. doi:10.4271/2003-01-3265.

[79] Dirrenberger, P., Glaude, P.-A., Bounaceur, R., Le Gall, H., da Cruz, A. P., Konnov, A. A., and Battin-Leclerc, F. *Laminar burning velocity of gasolines with addition of ethanol. Fuel*, 2014. volume 115:162–169.

[80] Teodosio, L., Bozza, F., Tufano, D., Giannattasio, P., Distaso, E., and Amirante, R. *Impact of the laminar flame speed correlation on the results of a quasi-dimensional combustion model for spark-ignition engine. Energy Procedia*, 2018. volume 148:631–638.

[81] Liang, L., Liang, L., Reitz, R. D., Reitz, R. D., Iyer, C. O., Iyer, C. O., Yi, J., and Yi, J. *Modeling Knock in Spark-Ignition Engines Using a G-equation Combustion Model Incorporating Detailed Chemical Kinetics. Sae*, 2007. volume 2007-01-01(724):776–0790. doi:10.4271/2007-01-0165.

[82] Singh, S., Liang, L., Kong, S.-C., and Reitz, R. D. *Development of a Flame Propagation Model for Dual-Fuel Partially Premixed Compression Ignition Engines. International Journal of Engine Research*, 2006. volume 7(1):65–75. ISSN 1468-0874. doi:10.1243/146808705X7464.

[83] Rakopoulos, C., Kosmadakis, G., Dimaratos, A., and Pariotis, E. *Investigating the effect of crevice flow on internal combustion engines using a new simple crevice model implemented in a cfd code. Applied Energy*, 2011. volume 88(1):111–126.

[84] Zhao, J. X. and Chia-fon, F. L. *Modeling of blow-by in a small-bore high-speed direct-injection optically accessible diesel engine.* Technical report, SAE Technical Paper, 2006.

[85] Tian, T., Noordzij, L., Wong, V., and Heywood, J. *Modeling piston-ring dynamics, blowby, and ring-twist effects. Journal of Engineering for Gas Turbines and Power*, 1998. volume 120(4):843–854.

[86] Reitz, R. D. and Kuo, T.-w. *Modeling of HC emissions due to crevice flows in premixed-charge engines. SAE Technical paper*, 1989. (892085).